



Article

Antimony (V) Adsorption at the Hematite–Water Interface: A Macroscopic and In Situ ATR-FTIR Study

Jerzy Mierzwa¹, Rose Mumbi¹, Avedananda Ray¹, Sudipta Rakshit^{1,*}, Michael E. Essington² and Dibyendu Sarkar³

¹ Department of Agricultural & Environmental Sciences, Tennessee State University, 3500 John A. Merritt. Blvd, Nashville, TN 37209, USA; jmierzwa@tnstate.edu (J.M.); rmumbi@tnstate.edu (R.M.); aray28@tnstate.edu (A.R.)

² Biosystems Eng. & Soil Science Department, University of Tennessee Knoxville, 2506 E.J. Chapman Dr, Knoxville, TN 37996, USA; messington@utk.edu

³ Department of Civil, Environmental and Ocean Engineering, Stevens Institute of Technology, Hoboken, NJ 07030, USA; dsarkar@stevens.edu

* Correspondence: srakshit@tnstate.edu; Tel.: +1-615-963-6058

Abstract: The environmental mobility of antimony (Sb) is largely unexplored in geochemical environments. Iron oxide minerals are considered major sinks for Sb. Among the different oxidation states of Sb, (+) V is found more commonly in a wide redox range. Despite many adsorption studies of Sb (V) with various iron oxide minerals, detailed research on the adsorption mechanism of Sb (V) on hematite using macroscopic, spectroscopic, and surface complexation modeling is rare. Thus, the main objective of our study is to evaluate the surface complexation mechanism of Sb (V) on hematite under a range of solution properties using macroscopic, in situ attenuated total reflectance Fourier transform infrared (ATR-FTIR) spectroscopic, and surface complexation modeling. The results indicate that the Sb (V) adsorption on hematite was highest at pH 4–6. After pH 6, the adsorption decreased sharply and became negligible above pH 9. The effect of ionic strength was negligible from pH 4 to 6. The spectroscopic results confirmed the presence of inner- and outer-sphere surface complexes at lower pH values, and only outer-sphere-type surface complex at pH 8. Surface complexation models successfully predicted the Sb (V) adsorption envelope. Our research will improve the understanding of Sb (V) mobility in iron-oxide-rich environments.

Keywords: adsorption; antimony; hematite; ATR-FTIR; mechanism; surface complexation modeling



Citation: Mierzwa, J.; Mumbi, R.; Ray, A.; Rakshit, S.; Essington, M.E.; Sarkar, D. Antimony (V) Adsorption at the Hematite–Water Interface: A Macroscopic and In Situ ATR-FTIR Study. *Soil Syst.* **2021**, *5*, 20. <https://doi.org/10.3390/soilsystems5010020>

Academic Editors: Evert Elzinga and Yuji Arai

Received: 29 January 2021

Accepted: 19 March 2021

Published: 21 March 2021

Publisher's Note: MDPI stays neutral with regard to jurisdictional claims in published maps and institutional affiliations.



Copyright: © 2021 by the authors. Licensee MDPI, Basel, Switzerland. This article is an open access article distributed under the terms and conditions of the Creative Commons Attribution (CC BY) license (<https://creativecommons.org/licenses/by/4.0/>).

1. Introduction

Elevated concentrations of antimony (Sb) in soil, sediments, and water bodies occur due to heavy mining operations and the subsequent use of antimony (Sb) in many industrial applications [1–3]. Another well-established contamination source has been linked to military and civilian shooting ranges. Antimony (Sb) is used as a hardening agent in lead bullets, and thus Sb is ultimately released into the environment when the bullets corrode [4,5]. Owing to the suspected carcinogenic effects of Sb in humans and other living organisms, the United State Environmental Protection Agency (USEPA) has declared Sb and its compounds as contaminants of emerging concern and set a maximum contamination level (MCL) value of 6 $\mu\text{g L}^{-1}$ for drinking water [6–8]. Indeed, greatly elevated concentrations of Sb in the soil (17,500 mg kg^{-1}) due to anthropogenic activities compared to background concentrations (0.05–0.22 mg kg^{-1}) have been reported [9].

Among the two major oxidation states (III and V) of Sb in the geochemical environments, Sb (V) is reported as the most dominant species prevalent in wide redox range (360 to –140 mV) while Sb (III) is considered to be more toxic [1,10–14]. In addition, the mobility and solubility of Sb (V) are greater than those of Sb (III) [12,13]. In shooting range soils, EXAFS characterization indicated that Sb (V) was the major species [15]. Macroscopic

and spectroscopic characterizations of soils and sediments have suggested that iron oxides, hydroxides, and oxyhydroxides are major sinks for Sb (V) species, and strong associations have been observed [14,16,17]. Consequently, many adsorption studies using pure iron mineral phases have been reported [10–13,17–20]. Macroscopic studies coupled with surface complexation modeling using goethite as a mineral indicate that Sb (V) has strong affinity for goethite and the adsorption is pH-dependent, where Sb (V) retention decreased drastically above pH 6 [10]. Leuz et al. proposed that the adsorption of Sb (V) on goethite occurred via a combination of inner-sphere and outer-sphere mechanisms. Tighe et al. (2005) [16] reported high affinity of amorphous $\text{Fe}(\text{OH})_3$ for Sb (V). In their study, the authors observed a sharp decrease of Sb (V) adsorption on amorphous $\text{Fe}(\text{OH})_3$ above pH 4 at an initial Sb (V) concentration of 23.4 μM . In contrast, no pH dependence was observed at lower initial Sb (V) concentrations ($\sim 0.234 \mu\text{M}$). Guo et al. (2014) [20] reported a similar decrease of Sb (V) adsorption (initial concentration range of 51–200 μM) above pH 6 for goethite and hydrous ferric oxide (HFO) minerals.

To enhance the understanding of the biogeochemical cycling of Sb, it is important that macroscopic characterization of adsorption process be coupled with direct spectroscopic evaluations. In situ attenuated total reflectance Fourier transform infrared (ATR-FTIR) spectroscopy has been accepted as an established means to investigate adsorption processes in real-time in the presence of water, provided the solute has IR-active bands that can change upon adsorption on solid surfaces [21–27]. Generally, the octahedral SbO_6 core of hexahydroxyantimonate $[\text{Sb}(\text{OH})_6^-]$ species has six normal modes of vibration, among which ν_3 and ν_4 modes are IR active [28]. These modes originate from $\nu(\text{Sb-O})$ antisymmetric stretch motions and $\delta(\text{Sb-O})$ bending motions [27]. The spectral signatures of these modes are in the undetectable regions ($680\text{--}230 \text{ cm}^{-1}$) of in situ ATR-FTIR spectra. However, the solid hexahydroxyantimonate salts showed distinctive $\nu(\text{O-H})$ stretching bands at 3220 cm^{-1} and $\delta(\text{O-H})$ and $\gamma(\text{O-H})$ deformation bands at 1105 and 735 cm^{-1} , respectively [27]. Indeed, a steady increase of the absorbance values of the IR bands at ~ 3200 and 1100 cm^{-1} was noticed when $\sim 100 \mu\text{M}$ Sb (V) had been adsorbed on amorphous iron oxide as a function of time (0–30 min) at pH 3 [27]. The authors reported strong pH dependence of the Sb (V) adsorption on amorphous iron oxide and concomitant inner-sphere and outer-sphere surface complexation. In a different study, Muller et al. (2015) [26] evaluated the competitive adsorption mechanism of As (V) and Sb (V) on six-line ferrihydrite and noted a similar sharp IR band at $\sim 1109 \text{ cm}^{-1}$ for Sb (V) adsorption at pH 3, which became broader and weaker as the pH increased.

Our main objective of this research is to evaluate the adsorption mechanism of Sb (V) on synthetic hematite, a common iron oxide in the environment, as a function of various solution properties using macroscopic, in situ ATR-FTIR spectroscopic experiments, and to apply surface complexation modeling to fit the adsorption edge data.

2. Materials and Methods

2.1. Reagent and Materials

Hematite ($\alpha\text{-Fe}_2\text{O}_3$) was synthesized using the methods described in Sugimoto et al. (1993) [29], by Elzinga and Kretzschmar (2013) [30], and in our earlier studies [31,32]. To summarize, a gel was formed by the slow addition of 500 mL of 2 M FeCl_3 solution over a period of 5 min to a continuously stirred 500 mL solution of 5.4 M NaOH. Then the gel was aged in a sealed Pyrex glass bottle at $101 \text{ }^\circ\text{C}$ for 8 days in an oven. After that, the dried product was cooled to room temperature and washed with Milli-Q water ($18.2 \text{ M}\Omega \text{ cm}$) until the electrical conductivity value reached $\sim <5 \mu\text{S cm}^{-1}$. After freeze-drying the cleaned suspension, X-ray diffraction (Rigaku, Woodlands, TX) was performed to confirm the mineral identity. The mineral was stored in a dry place at room temperature. Potassium hexahydroxyantimonate $[\text{KSb}(\text{OH})_6]$ was purchased from Sigma-Aldrich (St. Louis, MO, USA).

2.2. Antimony Sorption Experiments

Batch sorption experiments were carried out to determine the Sb (V) adsorption envelopes on hematite. The initial concentration of Sb (V) for sorption edge experiments was maintained at 8.21 μM ($1000 \mu\text{g L}^{-1}$) and was consistent with our previously published studies and environmentally relevant concentrations of Sb (V) [10,33]. The sorption-edge experiments were initiated in a 15 mL polypropylene centrifuge tube by adding appropriate amounts of Sb (V) stock solutions into a final 10 mL volume of overnight-equilibrated (24 h) hematite suspension at three different ionic strengths ($I = 0.001, 0.01, \text{ and } 0.1 \text{ M KCl}$) and at a pH range of 4–11. The pH was controlled by the addition of small volumes of 0.1 M HCl or NaOH, and the final pH value was recorded. The suspension was equilibrated for 24 h at 298 K. Preliminary kinetic experiments revealed a sorption equilibration time less than 1 h. After 24 h equilibration in an end-to-end shaker at 300 rpm, the final pH values for the suspension were recorded. Then the suspension was filtered using 0.22 μm syringe filter (Fischer Scientific, 09-730-19). The filtrates were analyzed for total Sb concentration using ICP-OES (iCAP 7400, Thermo Electron, West Palm Beach, FL, USA). The loss of Sb (V) was detected by the difference between the initial added Sb (V) (i.e., 8.21 μM) in the suspension and the amount of total Sb measured in the filtrate.

2.3. In Situ ATR-FTIR Experiments

To obtain molecular mechanisms of Sb (V) adsorption on hematite, in situ ATR-FTIR experiments were carried out using 45° ZnSe horizontal ATR (HATR) flow cell attachment as described in our earlier studies and in the other studies in the literature [22–25,31,32,34–36]. Extensive discussions on the flow cell set up and experimental system can be found in these cited references.

The effects on pH on the Sb (V) adsorption mechanism on hematite was evaluated by conducting an in situ ATR-FTIR pH envelope experiment. The experiment was started by initiating an equilibration step by circulating the background electrolyte solution (0.01 M KCl) through the hematite-coated sealed ZnSe HATR cell at a flow rate of 2 mL min^{-1} from a reaction vessel (500 mL total electrolyte volume) using a peristaltic pump (Watson Marlow 400, Falmouth, UK). The outlet of the solution from the flow cell was closed into the reaction vessel to maintain a constant reservoir volume. The reaction vessel was continuously purged with Ar to avoid interference from carbonate. The pH was recorded using a pH electrode inserted into the reaction vessel. The even mixing of the electrolyte solution inside the reaction vessel was ensured by the use of a magnetic stirring rod. Approximately 2 h was set for this preliminary equilibration step, in which background spectra were continuously collected averaging over 64 scans at a spectral resolution of 4 cm^{-1} . The pH was controlled throughout the equilibration step by adding small volumes of 0.1 M HCl or NaOH. The pH envelope experiment was started by adding an appropriate amount of Sb (V) stock solution into the vessel to reach an initial Sb (V) concentration of 5 μM . The pH was controlled at 5 (± 0.04). The spectra were collected for 1 h until no further increase of the IR band was noticed. Then, the pH was increased to the next value and these steps were continued until spectra were collected in a pH range of 5–8.

Infrared spectra of aqueous Sb (V) were also collected in a similar pH range (5–8) using a Ge ATR crystal to help interpret the Sb (V)-hematite adsorption spectra. The aqueous and adsorbed spectra of Sb (V) were plotted with absolute absorbance value at each pH value for comparing the increase of absorbance due to adsorption of Sb (V) on hematite. A similar comparison was also made by normalizing the aqueous and adsorbed Sb (V) spectra to determine the shape of the IR band irrespective of the absorbance value.

2.4. Surface Complexation Modeling

The 2 pKa formulation of the triple-layer surface complexation model (TLM) was used to describe the adsorption of Sb (V) on hematite as a function of pH. See Essington (2015) [37] for a detailed description of the TLM. The TLM views the solid–solution interface to consist of an inner Helmholtz layer for the adsorption of protons and species

complexed by inner-sphere mechanisms, an outer Helmholtz layer for the retention of species complexed by an outer-sphere mechanism, and a diffuse layer for counter-ion charge. The charge density in each of the inner and outer Helmholtz layers is proportional to the electrical potential in each layer, where the inner and outer layer capacitance values (C_1 and C_2) are the proportionality factors. The diffuse layer charge distribution is predicted using Gouy–Chapman double-layer theory. Adsorption reactions at the solid–solution interface are described by intrinsic equilibrium constants (K_{int} values), which are true constants at a fixed ionic strength. The C_1 , C_2 , and K_{int} values for proton adsorption and desorption and counter-ion complexation in the outer Helmholtz plane are fixed values in the TLM (Tables S1 and S2). Other fixed parameters included the equilibrium constants ($\log K$ values adjusted for ionic strength) that describe the aqueous speciation of Sb, the specific surface area (S_A), suspension density (a), and the counter-ion concentrations (0.001, 0.01, and 0.1 M KCl). The total site concentration (S_T) was an optimized parameter, as was the total site density (n_S , which was computed from S_T , S_A , and a).

The FITEQL 4.0 computer code was used to optimize the $\log K_{\text{int}}$ values for user-defined adsorption reactions by minimizing the variance between experimental and predicted Sb adsorption envelopes [38]. The measure of goodness-of-fit generated by FITEQL is V_Y , the weighted sum of squares of residuals divided by the degrees of freedom. In general, chemical models that produce V_Y values less than 20 are deemed acceptable, although the desired result is to identify a chemical model that generates the smallest value of V_Y , and is supported by a mechanistic interpretation of the experimental ATR-FTIR data. Several surface complexation reactions have been proposed to describe Sb retention at variable-charge surface functional groups [39–42]. Commonly, these include inner-sphere monodentate or bidentate and outer-sphere surface complexes, alone or in combination. The ATR-FTIR findings indicate that both inner- and outer-sphere Sb surface species are formed at the hematite surface.

Three surface complexation models were examined (Table 1). The models were applied independently to the three ionic strength conditions. Model I considered the formation of the inner-sphere complex $\equiv\text{FeOSb}(\text{OH})_4^\circ$ and the outer-sphere complex $\equiv\text{FeOH}_2^+ - \text{Sb}(\text{OH})_6^-$. Model II considered the formation of inner-sphere surface complex $\equiv\text{FeOSb}(\text{OH})_5^-$ and outer-sphere surface complex $\equiv\text{FeOH}_2^+ - \text{Sb}(\text{OH})_6^-$. Model III considered the formation of the inner-sphere surface complex $(\equiv\text{FeO})_2\text{Sb}(\text{OH})_3^\circ$ and the outer-sphere complex $\equiv\text{FeOH}_2^+ - \text{Sb}(\text{OH})_6^-$.

Table 1. The optimized triple layer surface complexation models that describe the adsorption of antimony by hematite as a function of pH and ionic strength.

Reaction	$\log K^{\text{int}} \dagger$		
	0.001	0.01	0.1
Model I			
$\equiv\text{FeOH}^0 + \text{H}^+ + \text{Sb}(\text{OH})_6^- = \equiv\text{FeOSb}(\text{OH})_4^\circ + 2\text{H}_2\text{O}$	8.56(0.10)	8.49(0.10)	8.42(0.10)
$\equiv\text{FeOH}^0 + \text{H}^+ + \text{Sb}(\text{OH})_6^- = \equiv\text{FeOH}_2^+ - \text{Sb}(\text{OH})_6^-$	10.80(0.14)	11.31(0.14)	11.41(0.09)
$V_Y \ddagger$	0.053	0.227	1.219
Model II			
$\equiv\text{FeOH}^0 + \text{Sb}(\text{OH})_6^- = \equiv\text{FeOSb}(\text{OH})_5^- + \text{H}_2\text{O}$	2.20(0.10)	2.42(0.53)	2.76(0.10)
$\equiv\text{FeOH}^0 + \text{H}^+ + \text{Sb}(\text{OH})_6^- = \equiv\text{FeOH}_2^+ - \text{Sb}(\text{OH})_6^-$	10.66(0.17)	11.11(0.27)	NC §
V_Y	0.142	0.161	0.703
Model III			
$2\equiv\text{FeOH}^0 + \text{H}^+ + \text{Sb}(\text{OH})_6^- = (\equiv\text{FeO})_2\text{Sb}(\text{OH})_3^\circ$	13.56(0.20)	14.19(0.20)	13.95(0.24)
$\equiv\text{FeOH}^0 + \text{H}^+ + \text{Sb}(\text{OH})_6^- = \equiv\text{FeOH}_2^+ - \text{Sb}(\text{OH})_6^-$	10.52(0.27)	10.72(1.0)	10.32(1.9)
V_Y	0.067	0.410	0.410

\dagger Common logarithm of the intrinsic surface complexation constants (standard deviation). \ddagger V_Y is the weighted sum of squares divided by the degrees of freedom. \S NC, the optimization procedure would not converge with this species considered.

3. Results and Discussion

3.1. In Situ ATR-FTIR Analysis of Sb (V) Adsorption on Hematite

The results from in situ ATR-FTIR experiments are presented in Figures 1–3. In Figure 1, the final spectra of hematite-adsorbed Sb (V) (5 μM) was stacked on top of aqueous Sb (V) (25 μM) spectra at pH values 5–8 to identify the increase of IR absorbance value due to the adsorption of Sb (V) on hematite. Study of $\sim 10 \mu\text{M}$ Sb (V) adsorption on minerals was considered consistent with mine effluent and environmentally relevant concentrations of antimony [1,2,26]. For measurements of aqueous Sb (V) FTIR spectra, a five times greater concentration (25 μM) was used in order to obtain a detectable signal. Generally, other researchers have used much higher concentrations of aqueous Sb (V) ($\sim 50 \text{ mM}$) to obtain detectable signals [26,27]. The increase of the absorbance value of the IR band in the Sb (V)-hematite adsorption spectra compared to the aqueous one is indicative of surface complexation (Figure 1). A strong infrared band at 1111 cm^{-1} was found at pH 5, which became weaker and broader and ultimately disappeared at pH 8. McComb et al. (2007) [27] identified this IR band ($\sim 1100 \text{ cm}^{-1}$ in their study) as an indicator of strongly adsorbed surface species of Sb (V) on iron oxide. The weak shoulder at 1015 cm^{-1} at pH 5, 6, and 7 became a broad peak at pH 8 (Figure 1). This IR band is a characteristic of in-plane O-H deformation [$\delta(\text{O-H})$] mode in aqueous Sb (V) salt [26,27]. Thus, this IR band is indicative of very weak surface interactions of Sb (V) with hematite. These findings are consistent with macroscopic adsorption data, in which the adsorption envelope of Sb (V) on hematite steeply decreased after pH 6 (Figure 4). Another way to investigate the characteristic IR band change due to adsorption can be done by comparing the normalized spectra of aqueous and adsorbed Sb (V) species (Figure 2).

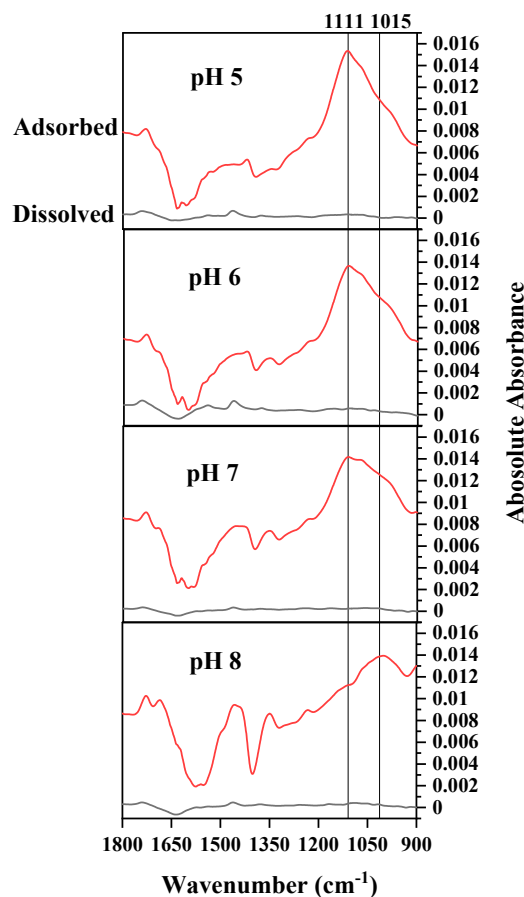


Figure 1. The in situ ATR-FTIR spectra of adsorbed and dissolved Sb (V) were stacked at each pH value. The intensity scale is drawn on actual scale obtained in the experiment.

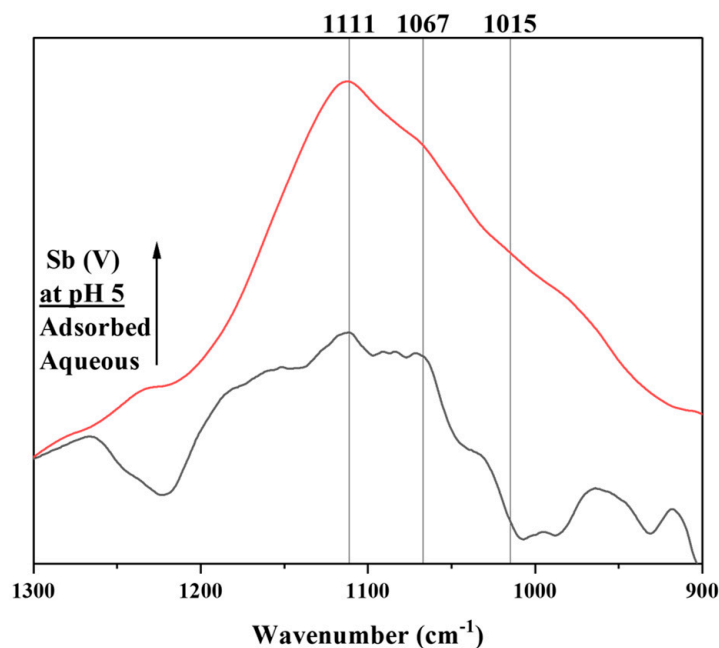


Figure 2. Normalized in situ ATR-FTIR spectra of adsorbed and dissolved Sb (V) at pH 5.

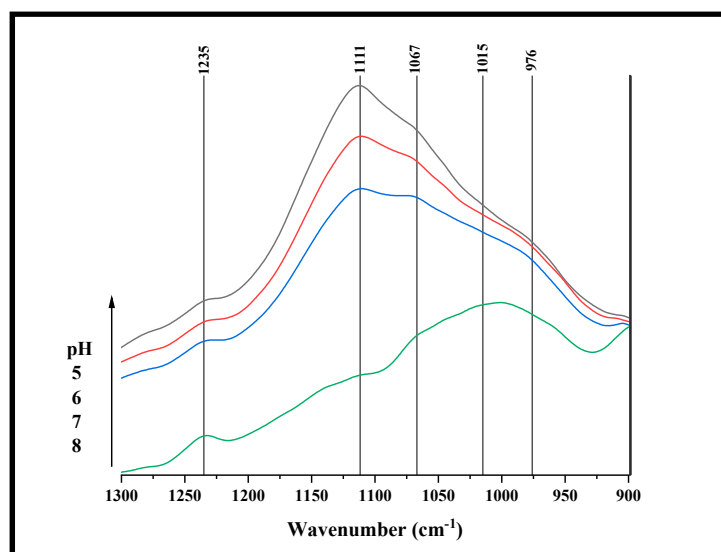


Figure 3. In situ ATR-FTIR spectra of hematite-adsorbed 5 μM Sb (V) collected at pH values 5–8.

An example of this type of comparison for pH 5 suggested a significant difference of the shape of the IR band at 1111 cm^{-1} (Figure 2). In addition, a shape change ($\sim 1069\text{ cm}^{-1}$) and shifts ($\sim 1015\text{ cm}^{-1}$) of the shoulders in the Sb (V)-hematite adsorption spectrum compared to the aqueous Sb (V) spectrum can be noticed at pH 5. Further, the Sb (V)-hematite adsorption spectra at pH 5–8 were stacked in the $900\text{--}1300\text{ cm}^{-1}$ wavenumber region to scrutinize the change in IR bands due to pH increase (Figure 3). In this comparison, the changes discussed based on Figure 1 were magnified in the $900\text{--}1300\text{ cm}^{-1}$ spectral region and the changes are consistent with previous discussions. Overall, the FTIR data indicate a combination of inner- and outer-sphere surface complexes at low pH values (5–7), which changed to outer-sphere surface complexation at pH 8. Weakening of the IR band ($\sim 1111\text{ cm}^{-1}$) assigned for inner-sphere surface complexation upon increasing pH was very clear (Figures 1 and 3). Below we use these spectroscopic results to hypothesize the possible surface complexes using thermodynamic-based surface complexation modeling.

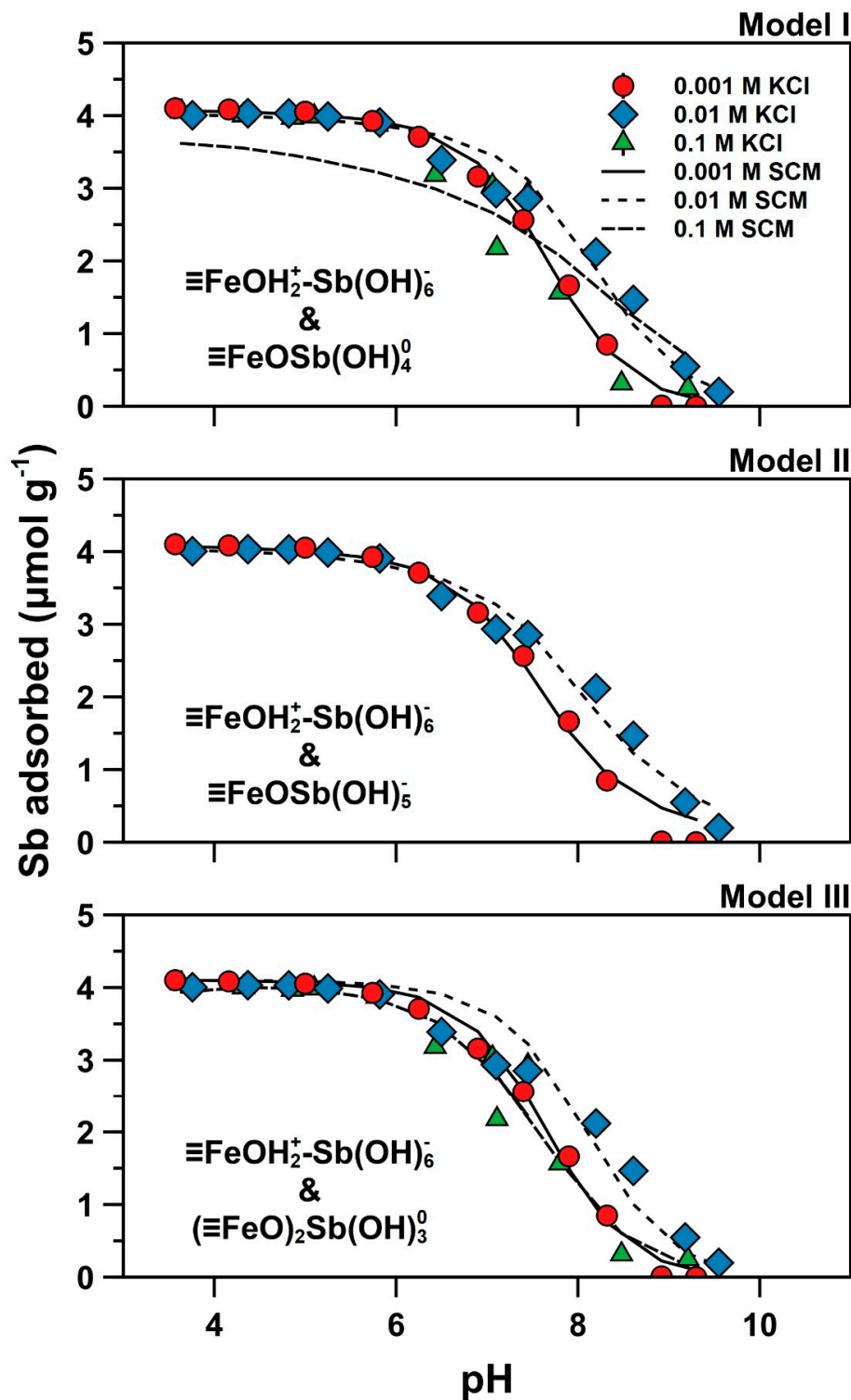


Figure 4. (A) (Top) Model 1. The experimental and predicted adsorption of Sb on hematite as a function of pH in 0.001, 0.01, and 0.1 M KCl ionic media. The surface complexation model assumes the formation of inner-sphere [$\equiv\text{FeOSb}(\text{OH})_4^0$] and outer-sphere [$\equiv\text{FeOH}_2^+-\text{Sb}(\text{OH})_6^-$] complexes. (B) (Middle) Model II. The experimental and predicted adsorption of Sb on hematite as a function of pH in 0.001 and 0.01 M KCl ionic media. The surface complexation model assumes the formation of inner-sphere [$\equiv\text{FeOSb}(\text{OH})_5^-$] and outer-sphere [$\equiv\text{FeOH}_2^+-\text{Sb}(\text{OH})_6^-$] complexes. (C) (Bottom) Model III. The experimental and predicted adsorption of Sb on hematite as a function of pH in 0.001 and 0.01 M KCl ionic media. The surface complexation model assumes the formation of bidentate inner-sphere [$(\equiv\text{FeO})_2\text{Sb}(\text{OH})_3^0$] and outer-sphere [$\equiv\text{FeOH}_2^+-\text{Sb}(\text{OH})_6^-$] complexes.

3.2. Adsorption Envelope and Surface Complexation Modeling

The adsorption envelope for Sb (V) with a concentration of 8.21 μM (1000 $\mu\text{g L}^{-1}$) indicated about 100–90% adsorption on hematite (2 g L^{-1}) at a pH range of 4–6 (Figure 4). The adsorption decreased steeply from pH 6.5 to 9 from a value of about 80% to below detectable levels. The behavior of the Sb (V)-hematite adsorption envelope followed a similar trend to other oxide minerals [10,33,40]. For example, Leuz et al. (2006) [10] found that between pH 3 and 6, about 96% of Sb (V) was adsorbed on goethite at ionic strength values of 0.1 and 0.01 M KCl. Beyond pH 6, a sharp decrease of Sb (V) adsorption was reported until pH 9 and ultimately reached below detectable levels at pH 12. However, compared to Leuz et al. (2006) [10], our sorption envelope data indicate minor ionic strength dependence above pH 6 (Figure 4). The trend of pH dependence of Sb (V) adsorption on hematite in our study is consistent with the observation of in situ ATR-FTIR experiments, in which the IR band at 1111 cm^{-1} at pH 5, indicative of strong inner-sphere surface complexation, gradually became broader and ultimately disappeared at higher pH value (pH = 8) (Figure 1). Conversely, the IR band at 1015 cm^{-1} , a characteristic in-plane O-H deformation [$\delta(\text{O-H})$] mode of aqueous Sb (OH) $_6^-$ species, became increasingly prominent by changing from a shoulder to a broad IR band as the pH increased to 8 (Figure 1). Building on the evidence from macroscopic adsorption envelope and in situ ATR-FTIR experiments, we conducted our surface complexation modeling (SCM) exercises to explain and model the sorption envelope.

In the literature, various surface complexation reactions have been proposed to describe Sb (V) retention at variable-charge surface functional groups [33,39–43]. Here we fit the adsorption envelope data using model I (assumes inner-sphere [$\equiv\text{FeOSb}(\text{OH})_4^\circ$] and outer-sphere [$\equiv\text{FeOH}_2^+ - \text{Sb}(\text{OH})_6^-$] complexes), model II (assumes inner-sphere [$\equiv\text{FeOSb}(\text{OH})_5^-$] and outer-sphere [$\equiv\text{FeOH}_2^+ - \text{Sb}(\text{OH})_6^-$] complexes), and model III (assumes bidentate inner-sphere [$(\equiv\text{FeO})_2\text{Sb}(\text{OH})_3^\circ$] and outer-sphere [$\equiv\text{FeOH}_2^+ - \text{Sb}(\text{OH})_6^-$] complexes) (Table 1). Model III performed somewhat better than model I for 0.1 M ionic strength (Figure 4). Thus, incorporating a bidentate inner-sphere surface complex in the model improved the fit at 0.1 M ionic strength. Use of the $\equiv\text{FeOSb}(\text{OH})_5^-$ monodentate surface complex instead of the $\equiv\text{FeOSb}(\text{OH})_4^\circ$ surface complex made model II not convergent for 0.1 M ionic strength data. Overall, all models predicted a ligand exchange reaction, in which a proton is consumed. Thus, the models are consistent with the adsorption envelope behavior, in which increasing pH decreased the adsorption of Sb (V). The occurrence of inner-sphere and outer-sphere surface complexes can be rationalized using the ATR-FTIR data presented in the previous section (Figures 1–3). However, specific stoichiometry or type (monodentate or bidentate) cannot be determined by ATR-FTIR spectroscopic data. Other researchers identified monodentate and bidentate surface complexes of Sb (V) on iron oxides using EXAFS [10,20].

Supplementary Materials: The following are available online at <https://www.mdpi.com/2571-8789/5/1/20/s1>, Table S1: Hematite and suspension parameters used in the triple-layer surface complexation modeling of antimony adsorption. Table S2. Aqueous speciation and proton and counter-ion adsorption reactions used in the triple-layer surface complexation modeling of antimony adsorption by hematite.

Author Contributions: Conceptualization, S.R., M.E.E., and D.S.; methodology, J.M., S.R., R.M., and A.R.; software, S.R.; validation, S.R.; formal analysis, S.R. and M.E.E.; investigation, J.M., S.R., and M.E.E.; resources, S.R.; data curation, S.R. and J.M.; writing—original draft preparation, S.R., J.M., and M.E.E.; writing—review and editing, S.R., M.E.E., and D.S.; visualization, S.R.; supervision, S.R.; project administration, S.R.; funding acquisition, S.R. All authors have read and agreed to the published version of the manuscript.

Funding: This research was funded by USDA NIFA Evans Allen, grant number TENX1413-CCAP.

Institutional Review Board Statement: Not applicable.

Informed Consent Statement: Not applicable.

Data Availability Statement: The data presented in this study can be found in the Supplementary Materials.

Acknowledgments: The authors acknowledge the support of College of Agriculture at Tennessee State University for supporting the facilities necessary for conducting this research.

Conflicts of Interest: The authors declare no conflict of interest.

References

1. Filella, M.; Belzile, N.; Chen, Y. Antimony in the environment: A review focused on natural waters: I. Occurrence. *Earth-Sci. Rev.* **2002**, *57*, 125–176. [[CrossRef](#)]
2. Filella, M.; Belzile, N.; Chen, Y.-W. Antimony in the environment: A review focused on natural waters: II. Relevant solution chemistry. *Earth-Sci. Rev.* **2002**, *59*, 265–285. [[CrossRef](#)]
3. Filella, M.; Belzile, N.; Lett, M.-C. Antimony in the environment: A review focused on natural waters. III. Microbiota relevant interactions. *Earth-Sci. Rev.* **2007**, *80*, 195–217. [[CrossRef](#)]
4. Carlin, J.F., Jr. *USGS Mineral Commodity Summaries*; USGS: Denver, CO, USA, 2000.
5. Clausen, J.; Korte, N. The Distribution of Metals in Soils and Pore Water at Three U.S. Military Training Facilities. *Soil Sediment Contam. Int. J.* **2009**, *18*, 546–563. [[CrossRef](#)]
6. Gebel, T. Arsenic and antimony: Comparative approach on mechanistic toxicology. *Chem. Biol. Interact.* **1997**, *107*, 131–144. [[CrossRef](#)]
7. Ilgen, A.G.; Trainor, T.P. Sb(III) and Sb(V) sorption onto Al-rich phases: Hydrous Al oxide and the clay minerals kaolinite KGa-1b and oxidized and reduced nontronite NAu-1. *Environ. Sci. Technol.* **2012**, *46*, 843–851. [[CrossRef](#)] [[PubMed](#)]
8. USEPA. *National Primary Drinking Water Regulations*; 816-F-09-004; USEPA: Washington, DC, USA, 2009.
9. Wilson, S.C.; Lockwood, P.V.; Ashley, P.M.; Tighe, M. The chemistry and behaviour of antimony in the soil environment with comparisons to arsenic: A critical review. *Environ. Pollut.* **2010**, *158*, 1169–1181. [[CrossRef](#)]
10. Leuz, A.; Hug, S.J.; Wehrli, B.; Johnson, C.A. Iron-mediated oxidation of antimony(III) by oxygen and hydrogen peroxide compared to arsenic(III) oxidation. *Environ. Sci. Technol.* **2006**, *40*, 2565–2571. [[CrossRef](#)]
11. Mitsunobu, S.; Harada, T.; Takahashi, Y. Comparison of antimony behavior with that of arsenic under various soil redox conditions. *Environ. Sci. Technol.* **2006**, *40*, 7270–7276. [[CrossRef](#)]
12. Mitsunobu, S.; Takahashi, Y.; Sakai, Y.; Inumaru, K. Interaction of synthetic sulfate green rust with antimony(V). *Environ. Sci. Technol.* **2009**, *43*, 318–323. [[CrossRef](#)] [[PubMed](#)]
13. Mitsunobu, S.; Takahashi, Y.; Terada, Y.; Sakata, M. Antimony(V) incorporation into synthetic ferrihydrite, goethite, and natural iron oxyhydroxides. *Environ. Sci. Technol.* **2010**, *44*, 3712–3718. [[CrossRef](#)]
14. Johnston, S.G.; Bennett, W.W.; Doriean, N.; Hockmann, K.; Karimian, N.; Burton, E.D. Antimony and arsenic speciation, redox-cycling and contrasting mobility in a mining-impacted river system. *Sci. Total Environ.* **2020**, *710*, 136354. [[CrossRef](#)] [[PubMed](#)]
15. Scheinost, A.C.; Rossberg, A.; Vantelon, D.; Xifra, I.; Kretzschmar, R.; Leuz, A.; Funke, H.; Johnson, C.A. Quantitative antimony speciation in shooting-range soils by EXAFS spectroscopy. *Geochimica Cosmochimica Acta* **2006**, *70*, 3299–3312. [[CrossRef](#)]
16. Tighe, M.; Lockwood, P.; Wilson, S. Adsorption of antimony(V) by floodplain soils, amorphous iron(III) hydroxide and humic acid. *J. Environ. Monit.* **2005**, *7*, 1177–1185. [[CrossRef](#)] [[PubMed](#)]
17. Burton, E.D.; Hockmann, K.; Karimian, N. Antimony Sorption to Goethite: Effects of Fe(II)-Catalyzed Recrystallization. *ACS Earth Space Chem.* **2020**, *4*, 476–487. [[CrossRef](#)]
18. Xi, J.; He, M.; Zhang, G. Antimony adsorption on kaolinite in the presence of competitive anions. *Environ. Earth Sci.* **2014**, *71*, 2989–2997. [[CrossRef](#)]
19. Xi, J.; He, M. Removal of Sb(III) and Sb(V) from aqueous media by goethite. *Water Qual. Res. J.* **2013**, *48*, 223–231. [[CrossRef](#)]
20. Guo, X.; Wu, Z.; He, M.; Meng, X.; Jin, X.; Qiu, N.; Zhang, J. Adsorption of antimony onto iron oxyhydroxides: Adsorption behavior and surface structure. *J. Hazard. Mater.* **2014**, *276*, 339–345. [[CrossRef](#)]
21. Hind, A.R.; Bhargava, S.K.; McKinnon, A. At the solid/liquid interface: FTIR/ATR—The tool of choice. *Adv. Colloid Interface Sci.* **2001**, *93*, 91–114. [[CrossRef](#)]
22. Lefèvre, G. In situ Fourier-transform infrared spectroscopy studies of inorganic ions adsorption on metal oxides and hydroxides. *Adv. Colloid Interface Sci.* **2004**, *107*, 109–123. [[CrossRef](#)]
23. Hug, S.J. In Situ Fourier Transform Infrared Measurements of Sulfate Adsorption on Hematite in Aqueous Solutions. *J. Colloid Interface Sci.* **1997**, *188*, 415–422. [[CrossRef](#)]
24. Hug, S.J.; Sulzberger, B. In situ Fourier Transform Infrared Spectroscopic Evidence for the Formation of Several Different Surface Complexes of Oxalate on TiO₂ in the Aqueous Phase. *Langmuir* **1994**, *10*, 3587–3597. [[CrossRef](#)]
25. Elzinga, E.J.; Sparks, D.L. Phosphate adsorption onto hematite: An in situ ATR-FTIR investigation of the effects of pH and loading level on the mode of phosphate surface complexation. *J. Colloid Interface Sci.* **2007**, *308*, 53–70. [[CrossRef](#)]
26. Muller, T.; Craw, D.; McQuillan, A.J. Arsenate and antimonate adsorption competition on 6-line ferrihydrite monitored by infrared spectroscopy. *Appl. Geochem.* **2015**, *61*, 224–232. [[CrossRef](#)]
27. McComb, K.A.; Craw, D.; McQuillan, A.J. ATR-IR Spectroscopic Study of Antimonate Adsorption to Iron Oxide. *Langmuir* **2007**, *23*, 12125–12130. [[CrossRef](#)]
28. Nakamoto, K. *Infrared and Raman Spectra of Inorganic and Coordination Compounds*; Wiley: Hoboken, NJ, USA, 1986.

29. Sugimoto, T.; Sakata, K.; Muramatsu, A. Formation Mechanism of Monodisperse Pseudocubic α -Fe₂O₃ Particles from Condensed Ferric Hydroxide Gel. *J. Colloid Interface Sci.* **1993**, *159*, 372–382. [[CrossRef](#)]
30. Elzinga, E.; Kretzschmar, R. In situ ATR-FTIR spectroscopic analysis of the co-adsorption of orthophosphate and Cd(II) onto hematite. *Geochimica Cosmochimica Acta* **2013**, *117*, 53–64. [[CrossRef](#)]
31. Rakshit, S.; Sallman, B.; Davantés, A.; Lefèvre, G. Tungstate (VI) sorption on hematite: An in situ ATR-FTIR probe on the mechanism. *Chemosphere* **2017**, *168*, 685–691. [[CrossRef](#)] [[PubMed](#)]
32. Sallman, B.; Rakshit, S.; Lefevre, G. Influence of phosphate on tungstate sorption on hematite: A macroscopic and spectroscopic evaluation of the mechanism. *Chemosphere* **2018**, *213*, 596–601. [[CrossRef](#)] [[PubMed](#)]
33. Rakshit, S.; Sarkar, D.; Datta, R. Surface complexation of antimony on kaolinite. *Chemosphere* **2015**, *119*, 349–354. [[CrossRef](#)]
34. Peak, D.; Ford, R.G.; Sparks, D.L. An in Situ ATR-FTIR Investigation of Sulfate Bonding Mechanisms on Goethite. *J. Colloid Interface Sci.* **1999**, *218*, 289–299. [[CrossRef](#)]
35. Parikh, S.J.; Mukome, F.N.; Zhang, X. ATR-FTIR spectroscopic evidence for biomolecular phosphorus and carboxyl groups facilitating bacterial adhesion to iron oxides. *Colloids Surf. B Biointerfaces* **2014**, *119*, 38–46. [[CrossRef](#)]
36. Dolui, M.; Rakshit, S.; Essington, M.E.; Lefèvre, G. Probing Oxytetracycline Sorption Mechanism on Kaolinite in a Single Ion and Binary Mixtures with Phosphate using In Situ ATR-FTIR Spectroscopy. *Soil Sci. Soc. Am. J.* **2018**, *82*, 826–838. [[CrossRef](#)]
37. Essington, M.E. *Soil and Water Chemistry: An Integrative Approach*; CRC Press: Boca Raton, FL, USA, 2015.
38. Herbelin, A.L.; Westall, J.C. *A Computer Program for Determination of Chemical Equilibrium Constants from Experimental Data*; Department of Chemistry, Oregon State University: Corvallis, Oregon, 1999.
39. Essington, M.E.; Vergeer, K.A. Adsorption of Antimonate, Phosphate, and Sulfate by Manganese Dioxide: Competitive Effects and Surface Complexation Modeling. *Soil Sci. Soc. Am. J.* **2015**, *79*, 803–814. [[CrossRef](#)]
40. Essington, M.E.; Stewart, M.A. Adsorption of Antimonate by Gibbsite: Reversibility and the Competitive Effects of Phosphate and Sulfate. *Soil Sci. Soc. Am. J.* **2016**, *80*, 1197–1207. [[CrossRef](#)]
41. Essington, M.; Stewart, M.; Vergeer, K. Adsorption of Antimonate by Kaolinite. *Soil Sci. Soc. Am. J.* **2017**, *81*, 514–525. [[CrossRef](#)]
42. Essington, M.E.; Stewart, M.A. Adsorption of Antimonate, Sulfate, and Phosphate by Goethite: Reversibility and Competitive Effects. *Soil Sci. Soc. Am. J.* **2018**, *82*, 803–814. [[CrossRef](#)]
43. Rakshit, S.; Sarkar, D.; Punamiya, P.; Datta, R. Antimony sorption at gibbsite-water interface. *Chemosphere* **2011**, *84*, 480–483. [[CrossRef](#)] [[PubMed](#)]